Article

Synthesis of a Novel Magnetic Biochar from Lemon Peels via Impregnation-Pyrolysis for the Removal of Methyl Orange from Wastewater

Samah Daffalla [1,2,*] , Enshirah Da'na [3], Amel Taha [4,5] and Mohamed R. El-Aassar [6]

[1] Department of Environment and Agricultural Natural Resources, College of Agricultural and Food Sciences, King Faisal University, P.O. Box 400, Al-Ahsa 31982, Saudi Arabia
[2] Department of Chemical Engineering, College of Engineering, University of Khartoum, Khartoum P.O. Box 321, Sudan
[3] Faculty of Engineering Technology, Al-Balqa Applied University, P.O. Box 15008, Amman 11134, Jordan
[4] Department of Chemistry, King Faisal University, P.O. Box 400, Al-Ahsa 31982, Saudi Arabia
[5] Department of Chemistry, Faculty of Science and Technology, Al-Neelain University, Khartoum P.O. Box 11121, Sudan
[6] Department of Chemistry, College of Science, Jouf University, P.O. Box 2014, Sakaka 72388, Saudi Arabia; mrelaassar@ju.edu.sa
* Correspondence: sbalal@kfu.edu.sa, Tel.: +966-135898731

Abstract: This research examined the elimination of methyl orange (MO) utilizing a novel magnetic biochar adsorbent (MLPB) derived from lemon peels via an impregnation-pyrolysis method. Material characterization was conducted using SEM, XRD, TGA, FTIR, and nitrogen adsorption isotherms. SEM-EDX analysis indicates that MLPB is a homogeneous and porous composite comprising Fe, O, and C, with iron oxide uniformly dispersed throughout the material. Also, MLPB is porous with an average pore diameter of 4.65 nm and surface area value (111.45 m^2/g). This study evaluated pH, MO concentration, and contact time to analyze the adsorption process, kinetics, and isothermal behavior. Under optimal conditions, MLPB was able to remove MO dye from aqueous solutions with an efficiency of 90.87%. Results showed optimal MO removal at pH 4, suggesting a favorable electrostatic interaction between the adsorbent and dye. To ascertain the adsorption kinetics, the experimental findings were compared using several adsorption models, first- and second-orders, and intra-particle diffusion. According to the findings, the pseudo-second-order model described the adsorption kinetic promoting the formation of the chemisorption phase well. Modeling of intra-particle diffusion revealed that intra-particle diffusion is not the only rate-limiting step. A study involving isothermal systems showed that Langmuir is a good representation of experimental results; the maximum adsorption capacity of MLPB was 17.21 mg/g. According to the results, after four cycles of regeneration, the produced magnetic material regained more than 88% of its adsorption ability.

Keywords: magnetic biochar; methyl orange; adsorption isotherms; adsorption kinetics; regeneration; breakthrough
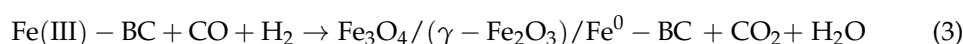
1. Introduction

Recently, environmentally friendly chemical processes that enable dye removal from wastewater have been attracting considerable attention in areas where water pollution is a major concern [1]. Hazardous and non-biodegradable organic dyes can cause cancer, mutagenesis, and teratogenetic effects and pose significant risks to human health and marine life [1,2]. In order to solve the ecological, biological, and industrial problems caused by dye discharge, dyes need to be properly removed from wastewater. Azo dyes are commonly employed as coloring agents in fabrics, inks, paints, and polymers [1–3]. There is a greater consumption of azo dyes in the textile industry than any other dye class due to their ease of application, minimal energy consumption, and availability of a wide

range of colors [4]. There are several problems associated with these dyes in wastewater, including aesthetic issues, effects on the demise of aquatic life, light penetration, and the photosynthetic activity of algae and aquatic plants [3,4]. The anionic dye methyl orange (MO) is an example of an industrially relevant toxic dye with known harmful effects on humans [5]. The removal of methyl orange has been carried out using numerous techniques, including precipitation, coagulation, flocculation, photodegradation, biological degradation, catalytic degradation, and adsorption [5].

In wastewater treatment, adsorption is considered one of the most effective techniques [3,5–7]. The reason is that it is simple, has a low cost, and requires less maintenance than other methods. It is also highly selective, consumes relatively few chemicals, is a fast kinetic, and is sensitive to dye concentrations even at low levels [5,6]. A wide range of adsorbents have been reported so far for the removal of methyl orange, including biochar, Anchote peel, magnetic clay biochar, activated carbon, nanocomposites, polymers, and many more [5–10]. In recent years, a potential class of useful compounds generated from biomass has surfaced: biochar (BC). Because of its high activity, porosity, adaptability, and affordability, biochar shows great promise as a catalyst substitute. BC, however, has limited application in wastewater treatment due to poor separation and regeneration [6,11,12]. Another worry is that BC discharged into natural waterways may increase the movement and resuspension of contaminants in sediments, which might lead to secondary contamination. Consequently, the development of magnetic biochar that addresses these drawbacks is essential to their continued industrial use. The use of magnetic biochar can greatly enhance performance [13].

Prior research has demonstrated that adding magnetic nanoparticles to the adsorbent would be a practical way to separate powdered small particles in solutions with external magnetic fields. This approach is more effective than standard centrifugation or filtration, especially when dealing with high-suspended solids or oil-contaminated water. Numerous magnetic adsorbents have been employed to eliminate diverse contaminants from water, such as heavy metals using magnetite zeolites, Pb^{2+} and tetrabromobisphenol from the aqueous phase by magnetite activated carbon, arsenic using magnetic graphene oxide, and lead, cadmium, and arsenic using magnetic biochar [14,15]. Furthermore, magnetic adsorbents can be simply separated by using the magnetic method from contaminated water [15].

There are now four ways to create magnetic biochar (MBC): solvothermal, chemical co-precipitation, reductive co-precipitation, and impregnation-pyrolysis [13]. Impregnation pyrolysis is now the most popular technique. Generally, impregnation-pyrolysis refers to the process of impregnating biomass in a magnetic precursor solution, followed by heat treatment in an anoxic environment. The magnetic precursor can become magnetic particles through the reduction of the gases generated during pyrolysis, while the biomass can be activated [13]. There will also be the production of aromatic hydrocarbons (PAHs), CO, H_2, CO_2, and CH_4. CO and H_2 are typical reducing gases [16]. The MBC reaction produced by impregnation-pyrolysis may be summed up as follows, based on earlier research that used ferric iron salt as a magnetic precursor [13,16]:

$$Fe^{3+} + BC \rightarrow Fe(III) - BC \tag{1}$$

$$BC \xrightarrow{\Delta,\ O_2-limited} CO_2 + CO + H_2 + CH_4 + \text{other products} \tag{2}$$

$$Fe(III) - BC + CO + H_2 \rightarrow Fe_3O_4/(\gamma - Fe_2O_3)/Fe^0 - BC + CO_2 + H_2O \tag{3}$$

The preparation of MBC is influenced by the pyrolysis temperature, the duration of pyrolysis, and the biomass-to-impregnated magnetic precursor ratio. However, the performance of MBC is mostly determined by the pyrolysis temperature. Certain research claims that temperature can influence the kind of magnetic material during pyrolysis. α-Fe_2O_3 will convert to Fe_3O_4 as the pyrolysis temperature rises from 300 °C to 450 °C, significantly increasing the magnetism of MBC [13]. In general, when the pyrolysis temperature goes

over 600 °C, iron oxides will progressively transform into zero-valent iron [13]. However, Chen et al. [17] noted that at 600 °C, Fe_3O_4 is the primary magnetic material of sludge MBC and that, at 1000 °C, it progressively transforms into FeO, losing its magnetism. Accordingly, the temperature at which the pyrolysis should take place should depend on the target magnetic species [13].

In Al Ahsa, Saudi Arabia, Hasawi lemons are farmed in large quantities. Lemon peel, one of the significant by-products of lemon processing, makes up around 20% of the entire fruit and can be utilized to create magnetic biochar materials, preventing resource waste and environmental contamination [18]. The usage of Hasawi lemons, particularly the peels, to create magnetic biochar is what makes this work novel. There are economic and environmental advantages to using Hasawi lemon peels as a precursor for magnetic biochar. This technique lowers waste disposal expenses and methane emissions by keeping agricultural waste out of landfills. It encourages a circular economy by substituting commercial activated carbon with renewable resources. By eliminating contaminants from water, magnetic biochar provides an economical and environmentally friendly substitute. Its magnetic characteristics make the process of separation and recovery easier. The procedure lowers the cost of garbage disposal, transportation, and collection. Feasibility is contingent upon several conditions, including local availability, energy prices, and effective production techniques. Thus, this study will be among the first to examine the effectiveness of magnetic biochar produced from Hasawi lemon peel using the impregnation-pyrolysis method at 600 °C pyrolysis temperature for 1 h and was successfully applied to eliminate MO from aqueous solutions. Methyl orange dye (MO) adsorption was investigated using batch and continuous studies. The intra-particle diffusion model, pseudo-first-order, and pseudo-second-order models were used to investigate the adsorption kinetics of MO. Using the Langmuir, Freundlich, and Dubinin–Radushkevich (D–R) isotherm models, the adsorption isotherms were predicted. Furthermore, the regeneration and reuse of adsorbent was studied.

2. Methodology

2.1. Chemical

Methyl orange (98% MO), iron(III) chloride ($FeCl_3$), nitric acid (HNO_3), Potassium hydroxide (KOH), and sodium hydroxide (NaOH) were supplied from Merck (Darmstadt, Germany).

2.2. Synthesis of Magnetic Biochar

Magnetic biochar was synthesized using the impregnation-pyrolysis method. Firstly, lemon peels (LP) were obtained from a nearby marketplace. Lemon peels were completely rinsed with distilled water, dried, and then ground into small particles. A particle size range of 125–250 μm was chosen. Secondly, the LP samples were treated with 1 M $FeCl_3$ at room temperature for 1 h using a magnetic stirrer. Subsequently, hydrolysis and Fe^{3+} precipitation will be accelerated at 100 °C for 1 h. A certain quantity of LP (about 10 g) was then put in a ceramic crucible and pyrolyzed in a tube furnace at a heating rate of 10 °C/min to produce the magnetic biochar. During the pyrolysis and cooling process, nitrogen (N_2) gas was used as the purging gas in an oxygen-free atmosphere at a flow rate of 150 mL/min. The pyrolysis holding time was 1 h, and the temperature was set at 600 °C. According to the literature, the chosen temperature was one of several input series used to determine the ideal conditions for producing biochar from biomass [19,20]. By doing this, ferric iron that was previously absorbed in the feedstock can be transformed into magnetic material during pyrolysis (Equations (1)–(3)), as hydrogen is released during the pyrolysis process, which produces syngas from the breakdown of hemicellulose and cellulose. The pyrolysis yield of magnetic biochar was 34.4%. The magnetic biochar obtained was referred to as MLPB. Next, the sample was calcined for 4 h at 200 °C.

2.3. Instrument Analysis

At a wavelength of 4000–400 cm^{-1}, Fourier transform infrared spectroscopy (Cary 630 FT-IR Spectrophotometer model) was utilized to determine the surface functional groups of the samples. To examine the samples' morphology, scanning electron microscopy (SEM model FEI, QUANTA FEG, 250, Hillsboro, OR, USA) was employed. An analyzer model for surface area and pore size Utilizing nitrogen sorption at −196 °C, Micromeritics ASAP 2020 was utilized to evaluate the MLPB's surface area and pore size distribution. Using X-ray diffraction (model D8 Advance), the samples' chemical and crystalline constituents were determined. For one hour, diffraction was carried out across a range of 2θ at 40 kV and 40 mA. Using a TG-DTG (Perkin Elmer, Shelton, CT, USA) with a heating rate of 10 °C/min from 30 to 800 °C in a nitrogen (N$_2$) environment, thermal gravimetric analyses (TGA) of samples were carried out.

2.4. Experimental Procedures

Numerous parameters' impacts on dye removal were examined in a batch mode. The concentration (20–80 mg/L), pH (2–10), and MLPB dose (0.025–0.15 g) were among these parameters. Either 0.1 M NaOH or 0.1 M HNO$_3$ was added to the solution to change its pH. The flasks were shaken for the required time period using a thermostatic shaker. The kinetic studies were performed at 120 rpm and 25 °C in flasks with MLPB and a fixed concentration of MO dye (20 mg/L) for varying periods (0–60 min). After taking the flask out of the mixer at a specific time, the suspension was filtered using a Whatman syringe filter. In the filtered sample, MO concentrations were determined at 464 nm using a UV-Vis spectrophotometer (Shimadzu, Tokyo, Japan). A 24 h equilibrium study of 0.1 g MLPB with various MO solutions was conducted under 25 °C shaking with initial MO concentrations (20–80 mg/L).

The dye-laden MLPB was initially desorbed with 0.1 M KOH in order to assess its reusability. After that, distilled water and 0.1 M HNO$_3$ were added to the adsorbent until a pH of about 7.0 was reached. Regeneration and reuse of fourth-cycle adsorption-desorption adsorbents were investigated. Every experiment was carried out in duplicate. MO's adsorption capacity and dye removal efficiency were calculated using Equations (4) and (5).

$$\text{Removal efficiency of MO} = \frac{(C_i - C_t)}{C_o} \times 100 \qquad (4)$$

$$\text{Amount adsorbed } (q_t) = \frac{(C_i - C_t)V}{W}, \left(\frac{\text{mg of adsorbate}}{\text{g of adsorbent}}\right) \qquad (5)$$

where V is the volume (L), W is the mass of the MLPB (g), and C_i and C_t (mg/L) are the influent and effluent concentrations (mg/L).

To assess MLPB's efficacy in a real setting and minimize sorbent loss and clogging during operation, the material was layered between glass wool as a support layer. The column was 11 cm in length and 1.4 cm in diameter. With an initial pH of 3.0 and 0.6 g (bed height 1 cm) of MLPB, MO starting concentrations of 20, 50, and 80 mg/L were utilized at a flow rate of 0.65 mL/min. Samples were extracted and examined from the packed bed's bottom. The maximum absorption capacity (q_{total}, mg) for a particular intake concentration and flow rate may be found using the area under the plot of the adsorbed MO concentration [21]:

$$q_{total} = \frac{FA_r}{1000} = \frac{F}{1000} \int_{t=0}^{t=t_{total}} (C_i - C_t)dt \qquad (6)$$

where F, A_r, and t_{total} stand for flow rate (mL/min), the area under the curve (area), and total flow time (min), respectively.

The following equation can be used to calculate the equilibrium uptake ($q_{e,exp}$, mg/g):

$$q_{e,\,exp} = \frac{q_{total}}{x} \qquad (7)$$

where x is the adsorbent's mass (in grams) in the bed.

By calculating the volume occupied by the adsorbent (MLPB) and its overall volume, the porosity of a packed bed column may be computed. Here's how to go about it [22]:

$$V_{Column} = \pi r^2 L \tag{8}$$

$$V_{\text{MLPB}} = \frac{m_{\text{MLPB}}}{\rho_{\text{MLPB}}} \tag{9}$$

$$\text{Total Porosity } (\varepsilon_{total}) = \frac{V_{void}}{V_{column}} \tag{10}$$

where the total volume of the column (cm^3), the total volume of the MLPB (cm^3), the void volume of the column (cm^3), which is equal to ($V_{Column} - V_{BPBC}$), the total mass of the MLPB (g), the bulk density of the MLPB (g/cm^3), the radius of the column (cm), and the height of the column (cm), are V_{Column}, V_{MLPB}, V_{void}, m_{MLPB}, ρ_{MLPB}, r, and L, respectively.

3. Results and Discussions

3.1. Characterizations

3.1.1. FTIR Analysis

FTIR spectra of PL and MPLB are shown in Table 1 and Figure 1. Many functional groups are observed in the spectrum of the PL sample. These spectra revealed either a decrease, disappearance, or widening of the peaks following the impregnation-pyrolysis process. According to the long bandwidth around 3292 cm^{-1} on PL, O–H stretching vibrations of hydroxyl functional groups, including hydrogen bonds, were the predominant functional group [23]. Other significant peaks were found at bandwidths of 2090, 2088, 1710, 1597, and 1010 cm^{-1}, which were attributed to the stretching vibrations of hemicelluloses [24], alkyne groups [23], lactones, ketones, and carboxylic anhydrides [23], C=C aromatic ring vibrations from lignin [24], and C–O stretching [25]. The FTIR spectra of MLPB (Figure 1) showed a decrease in relative intensity, which was mostly caused by the disintegration of carboxyl groups at ranges between 4000 and 2000 cm^{-1}. At 1547 cm^{-1}, there could be some somewhat stable aromatic molecules and/or graphitic structures, indicating some relatively stable aromatic compounds [24]. The strong volatile release during pyrolysis and the loss of functional groups were linked to the disappearance or shifting of observable structural characteristics [26]. The peak at 1010 and 1710 cm^{-1}, which are associated with the stretching of C–O and C=O, decreased or disappeared when comparing MLPB and LP, proving that the pyrolysis process caused the hemicellulose, lignin, and cellulose that were present in the lemon peels to be depolymerized and destroyed [26]. In agreement with previous studies, metal–oxygen stretching frequencies usually occur between 500 and 600 cm^{-1} [27,28]; the characteristic Fe–O bond appeared at 642 cm^{-1} was observed.

Table 1. FTIR spectrum band assignment for PL and MPLB.

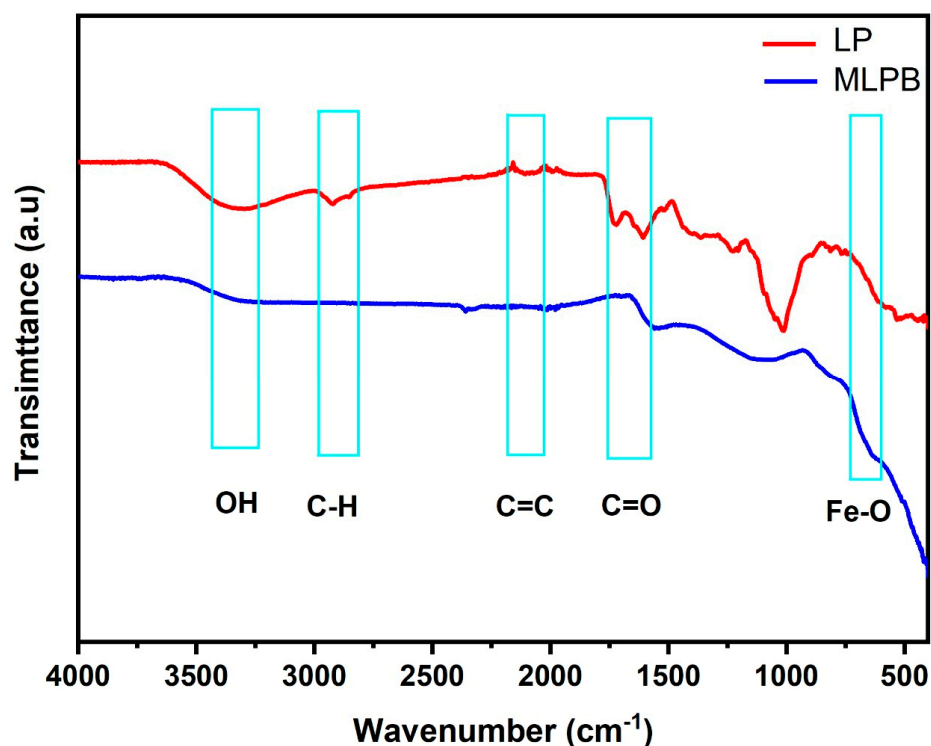| Assignment	Band Position (cm^{-1})	
	LP	MLPB
O–H stretching of hydroxyl group	3292	-
C–H stretching vibration from hemicelluloses	2920	-
C≡C stretching of alkyne group	2088	-
C=O stretching of lactones, ketones, and carboxylic anhydrides	1710	-
C=C aromatic ring vibrations from lignin	1597	1547
C–O stretching	1010	1105
Fe–O	-	642

Figure 1. MLPB and LP's FT-IR spectrum.

3.1.2. SEM Analysis

Table 2 contains the element composition analysis of the LP and MLPB samples, comparing their surface morphology and surface element content. Figure 2 displays the SEM images of the samples. The LP's surface is rough and uneven, as seen by the SEM scan (Figure 2a). MLPB, however, is characterized by its porous texture, and the surface is covered with iron oxide particles (Figure 2b). In pyrolysis, char surfaces act as nucleating and precipitating surfaces for iron oxide particles. As a result, both α-Fe_2O_3 and Fe_3O_4 particles are partially embedded in the biochar matrix, indicating good mechanical bonding that prevents their separation from the biochar matrix [29,30]. MLPB's rugged morphological structure was maintained by iron oxide particles dispersed on its surface (Figure 2b). The elements distributions on MLPB surface regions were mapped by SEM-EDS, as shown in Figure 2c–e. The presence of the intensely colored areas proves that the MLPB surface area is mostly composed of C, O, and Fe. It was evident that Fe has been efficiently loaded onto the MLPB by 24% (Table 2). The changes in the surface structure of the MLPB can increase its specific surface area, thereby providing more potential sites for MO adsorption.

Table 2. Element composition of LP and MLPB.

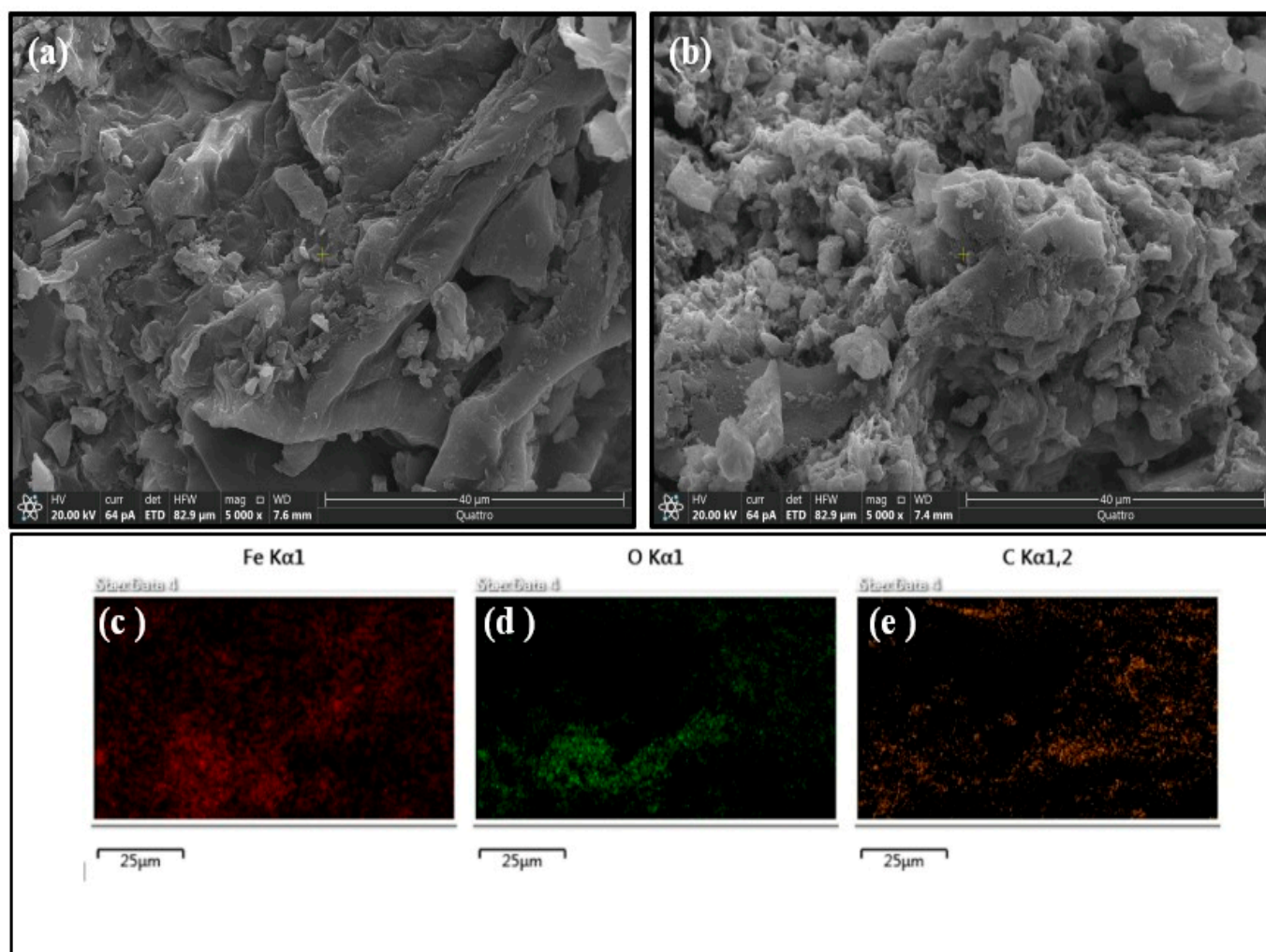| Adsorbents	Element Composition (%)		
	C	O	Fe
LP	57.0	41.9	-
MLPB	37.1	28.8	24.0

Figure 2. SEM images of (**a**) LP, (**b**) MLPB, and (**c**–**e**) C, O, and Fe; elemental distribution over the same region mapped per each element.

3.1.3. XRD Analysis

Iron oxides offer a variety of magnetic properties, which significantly depend on the shape and size of particles. These parameters, to a great extent, are governed by synthetic methods. Different methods have been reported for the preparation of magnetite nanoparticles. Here, magnetite nanoparticles were prepared and synthesized using the impregnation-pyrolysis method by pyrolyzing ground lemon peels in an oxygen-free furnace at a pyrolysis temperature of 600 °C. As a result of high temperature, particles heat up, undergo phase transformations, and some rhombohedral elementary cells of α-Fe_2O_3 hematite transform into Fe_3O_4, which were confirmed by XRD analysis [31]. The crystal phases of iron oxide nanoparticles were determined using the X-ray diffraction (XRD) technique. Figure 3 shows the appearance of numerous phase peaks for iron oxide in the 2θ range (0–80). The results verified the presence of characteristic peaks of both α-Fe_2O_3 and Fe_3O_4 nanoparticles on the LPB surface [32]. The main peaks at 24.0, 27.0, 33.40, 35.60, 40.10, 49.60, 54.02, 62.60, and 64.01 are assigned to the index at (012), (205), (104), (110), (113), (024), (116), (214), and (300), respectively. The peaks at 24.0, 33.07, 35.44, 40.78, 49.38, 54.03, 62.48, and 64.01 agreed with (JCPDS file No. 330-0664), confirming the crystallinity of (α-Fe_2O_3) on LPB [33]. The figure also shows the presence of other peaks with their indexed plane on LPB at 30.04 (220), 35.60 (311), 43.02 (400), 54.20 (422), 56.10 (511), and 62.40 (440). These peaks are also in agreement with the crystalline diffraction pattern of

Fe_3O_4 (JCPDS file No. 75-0033) matched magnetite [33]. Dewage et al. [32] obtained the same result by impregnating $FeCl_3$ on pyrolyzed Douglas fir biochar.
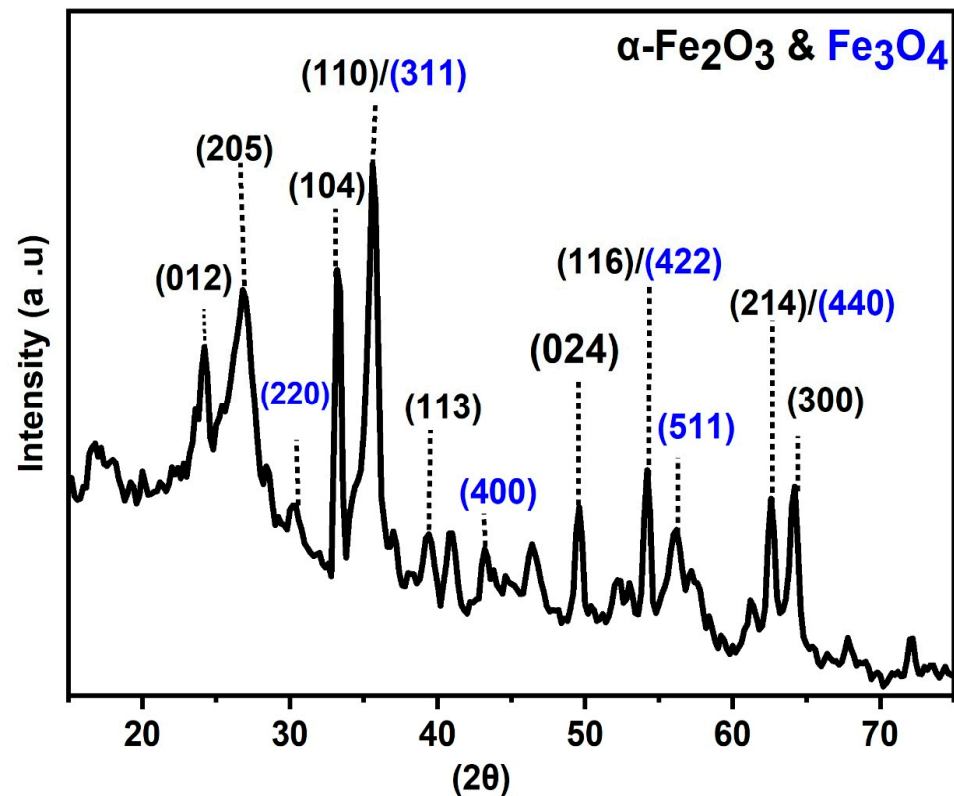

Figure 3. XRD patterns of MLPB.

3.1.4. TGA Analysis

The thermogravimetry diagram (TGA) of lemon peel (LP) and magnetite lemon peel is shown in Figure 4. The TGA thermogram of LP shows three stages of thermal decomposition. Firstly, there is a minor weight loss of 4% up to 200 °C, which is attributed to the loss of moisture and light volatile content. A second stage, in LP, showed a 34.3% mass loss occurring at the range of 300–400 °C, which was associated with the pyrolysis of lignin and cellulose. This stage was absent for MLPB due to the pyrolysis process in which the hemicellulose had been broken down [32]. The third stage shows weight loss for both samples up to 500 °C, which could be related to the decomposition of the lattice structure. From the thermogram of MLPB, two stages of thermal decomposition were observed. The first stage, with a loss of mass loss of about 10%, can be explained mainly by the release of water molecules and light volatile content of the MLPB. Further, the LMPB was almost stable up to 400 °C. Compared to the LP sample, this could be due to the thermal decomposition resistance capacity for iron oxides [34]. The second decomposition stage was observed at 428 °C. This could be due to the carbonization of biochar. Thus, it is obvious that the total weight loss of MLPB was lower compared to the LP, which could be explained by the presence of iron oxide nanoparticles' capacity to resist thermal decomposition. The obtained result is in agreement with Hosny et al. [34].
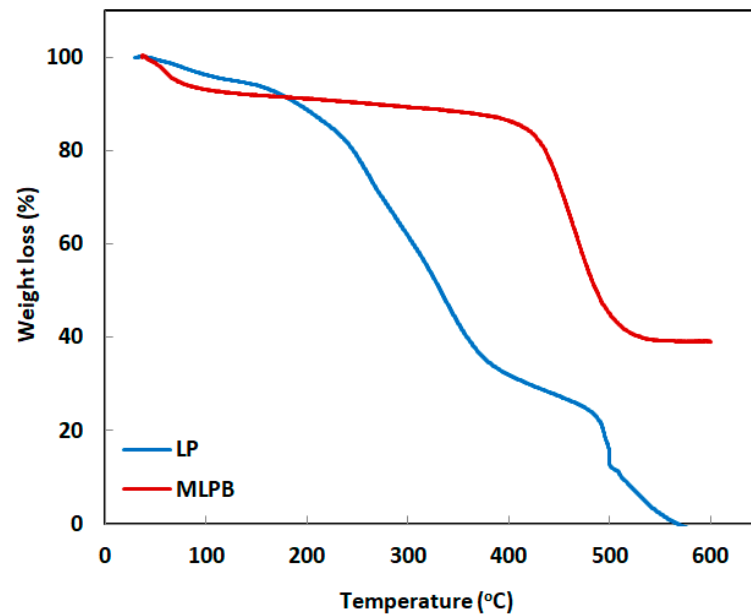
Figure 4. TGA curves of LP and MLPB.

3.1.5. BET Analysis

Figure 1 illustrates the MLPB hysteresis loop. The MLPB displayed type IV isotherms with an H3 hysteresis loop, which is common to mesoporous and microporous materials. (Figure 5a), according to the IUPAC classification [35]. It is actually true that when the temperature of pyrolysis rises over 550 °C, the size of the mesopores increases, and new micropores develop [36]. With a total pore volume of 0.091 cm^3/g and an average pore diameter of 4.65 nm, MLPB has a surface area of 111.45 m^2/g. A plot of the BJH pore size distribution is also shown in Figure 5b. The MLPB surface was found to have a mesoporous structure centered around 4 and 2.2 nm according to the BJH method (Figure 5b). The treatment process is ideal for adsorption since it has a lot of mesoporous sites [36].
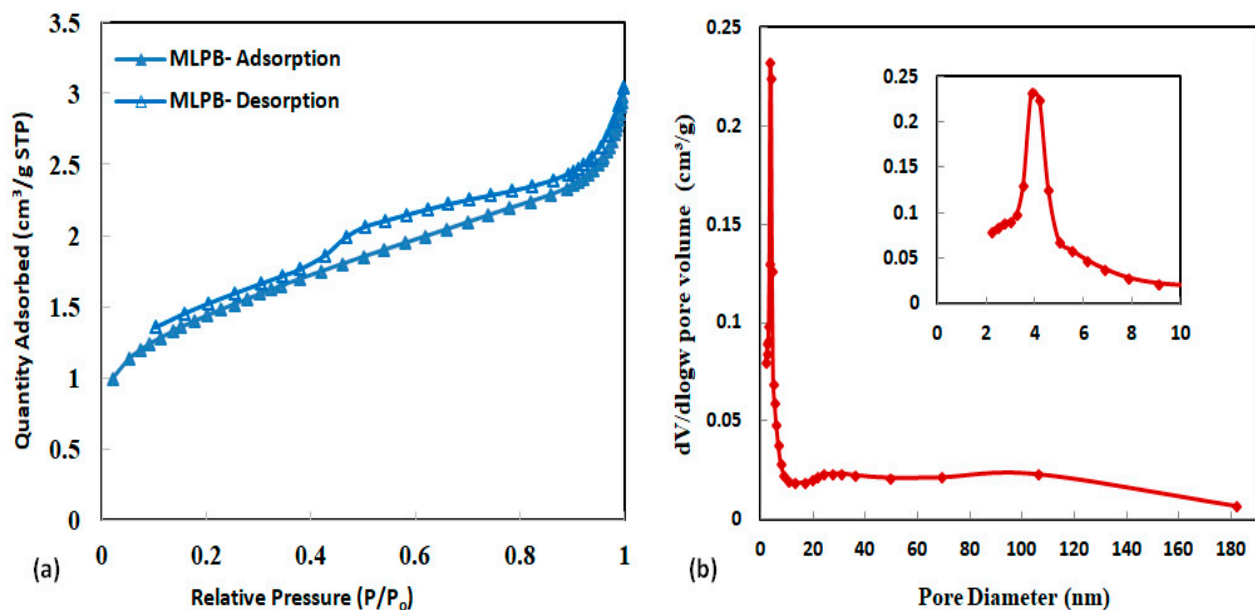

Figure 5. The MLPB sample's (**a**) N_2 absorption/desorption isotherms and (**b**) pore size distribution plot.

3.2. Adsorption Studies

Different factors can affect the adsorption performance of MLPB, such as pH, hardness, and the presence of other ions. MO is a model of anionic dyes in which they are adsorbed more over the materials with more positive charges on their surfaces; they are also adsorbed more at a low pH when the surface is positively charged. It also can affect the adsorption mechanism and the dissociation of dye molecules. In this paper, we focus on studying the influence of pH, initial concentration, adsorbent dose, and contact time.

3.2.1. Effect of Adsorbent Type on MO Uptake

For 24 h, at pH 3.0 and 25 °C, the adsorption capabilities of MO at a concentration of 20 mg/L were assessed for MLPB and lemon peels. The adsorbents were each used at a dosage of 0.1 g. Compared with lemon peels (q_e = 0.54 mg/g), MLPB displayed an approximately sevenfold higher adsorption capacity (q_e = 3.51 mg/g). Consequently, MLPB's performance was considered better, and it was chosen for further study.

3.2.2. Influence of pH

Since pH affects both the MPLB adsorbent's surface characteristics and the MO molecules' dissociation process in aqueous environments, adsorption processes are highly sensitive to pH levels. A pH range of 2.5 to 10.0 and an initial MO concentration of 20 mg/L were used to investigate the impact of pH on MPLB adsorption capability. The effect of pH on MPLB adsorption capacity is seen in Figure 6. The adsorption capacity of MPLB for dye adsorption slightly improves from 3.5 to 3.6 mg/g, and its removal efficiency also improves from 87.8 to 90% when the pH value is raised from 2.5 to 4.0. As the pH increases from 4 to 10, the dye adsorption and removal efficiency gradually decrease from 3.60 to 2.76 mg/g and 90 to 69%, respectively. With higher pH values, MPLB's negatively charged surface and anionic MO's repulsion suppress adsorption due to ionic repulsion [37,38]. As the MPLB adsorbent surfaces become positively charged at low pH values, more electrostatic attraction occurs between its surface and the negatively charged MO anions, increasing the capacity for adsorption. However, when the pH is very acidic, electrostatic repulsion happens between the positively charged active surface of MPLB and the protonated MO. As a result, it can be demonstrated that pH 4 is ideal for MO adsorption. The MO adsorption on magnetic AC produced similar outcomes [38].
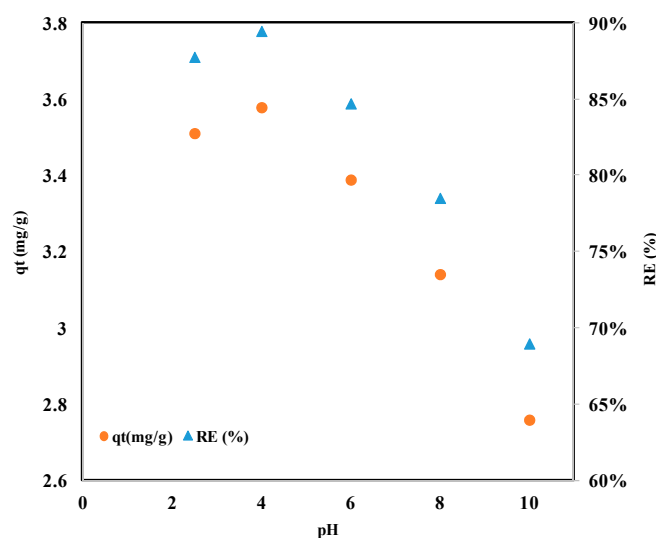

Figure 6. Impact of initial pH solution on MO's ability to adsorb onto MLPB (20 mg/L starting Mo concentration, 0.1 g adsorbent dosage).

3.2.3. Effect of Dosage of Adsorbent

An essential parameter in adsorption studies is the amount of adsorbent used, as it determines how much dye solution will be absorbed by a given quantity of adsorbent. Figure 7 demonstrates the effect of the MLPB dose on MO adsorption, ranging from 0.025 to 1.5 g. Initially, 15 mg/g of MO adsorption capacity was observed, but it decreased to 1.9 mg/g as the initial MLPB was increased. Increased MLPB doses lead to more entanglement of the MLPB in the solution, which results in adsorption in the interlayer space and a decrease in dye aggregation at the external surface. As a result, the adsorption capacity decreased with increasing MLPB dosage. Further, high MLPB dosages can alter the physical properties of solid–liquid suspensions, such as increasing viscosity and inhibiting dye molecules' diffusion across the surface. Because the concentration of MO was fixed, as the MLPB dosage increased, the adsorption capacity decreased [39,40].
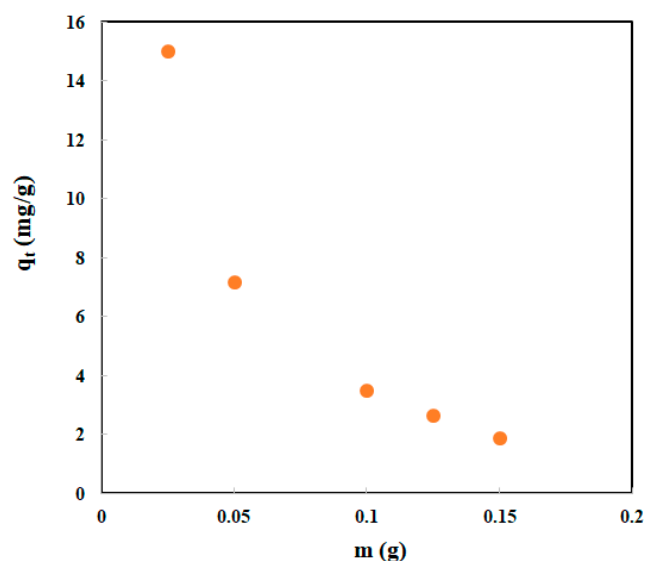

Figure 7. The impact of the MLPB dosage on the MO adsorption capacity at pH 3 and the starting Mo concentration of 20 mg/L.

3.2.4. Influence of Initial Concentration

Figure 8 illustrates the effect of different MO concentrations, varying from 10 to 80 mg/L at pH 3, 0.1 g of adsorbent, and 25 °C. This figure makes it clear that the initial concentration significantly affects the MO molecules' ability to adsorb. The q_e increased by almost 6 (from 1.82 mg/g to 12.17 mg/g) with an increase in dye concentration from 10 mg/L to 100 mg/L, suggesting a linear connection between q (mg/g) and C(mg/L). Increasing the starting concentrations (C_o) might explain the higher absorption capacity by amplifying the concentration gradient and facilitating the transport of MO molecules from the bulk solution to the MLPB surface. Consequently, quicker kinetics and a larger adsorption capacity are obtained by lowering the mass transfer resistance at high starting concentrations [41]. On the other hand, elimination efficiency decreased from 91% to 76% when the starting concentration increased from 10 mg/L to 80 mg/L. At larger starting concentrations, the adsorption sites on the surface of MLPB become saturated, which results in this behavior. Adsorption sites, therefore, become the limiting factor, while MO becomes the surplus component. Remediation efficiency is decreased with larger C_o values because the MLPB surface's ability to receive dye molecules diminishes while the number of active sites stays constant [41]. In order to be successful in commercial applications, initial dye concentrations should be optimized to guarantee realistic removal rates and maximize adsorption efficiency. Increasing the quantity of adsorbent to increase the number of accessible adsorption sites is one potential way to get around this restriction, as seen in Figure 8. Similar findings were documented by Kubendiran et al. [42] and Han et al. [43].
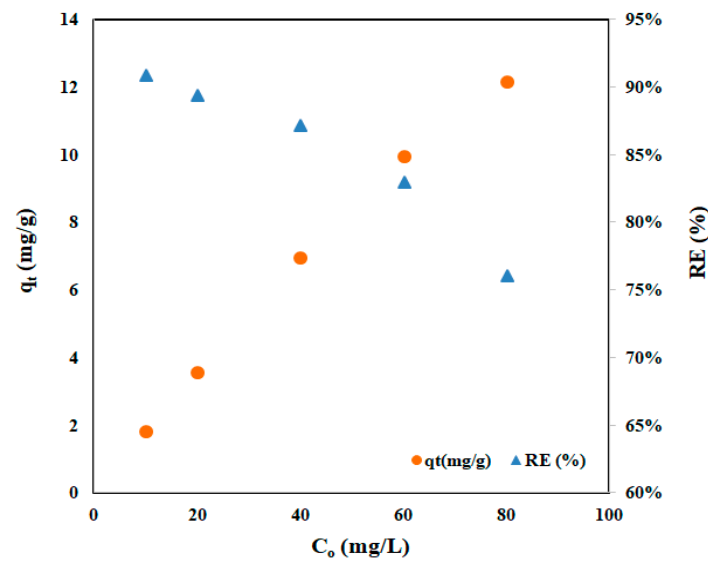
Figure 8. Effect of initial dye concentration of adsorption of MO dye unto MPLB at pH 3, 25 °C, and 0.1 g adsorbent dose.

3.2.5. Evaluation of Adsorption Kinetics

Figure 9 shows the batch adsorption of MO at different initial MO concentrations (20, 40, and 60 mg/L) in response to contact time. Results showed that all concentrations showed a significant increase in adsorbate uptake in the initial stage of contact time. With an initial MO concentration of 20, 40, and 60 mg/L, more than 94, 66, and 52% of MO was adsorbed in the first 35 min, respectively. Adsorption is fast at first (contact time), but it slows down later. This could be because there were many empty surface sites available during the first stage of adsorption, and it was difficult to fill the remaining empty surface sites due to the repelling forces that exist between the bulk phase and the dye molecules on the MLPB [23,39,44]. Additionally, the creation of a monolayer coating of dye molecules on the MLPB surface is confirmed by a continuous, smooth pattern toward saturation [23,39].
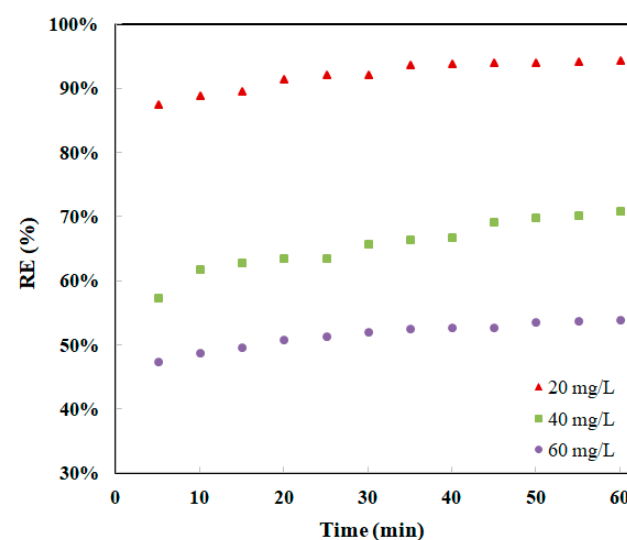

Figure 9. Impact of initial dye concentration and contact duration on MO dye adsorption onto MPLB at pH 3, 25 °C, and 0.1 g adsorbent dosage.

In an adsorption process, solutes are transported from liquid to the adsorbent surface by means of mass transfer. MO adsorption on MLPB was investigated using three of the most used kinetic models: pseudo-first-order, pseudo-second-order, and intra-particle

diffusion kinetics. By utilizing the correlation coefficient values (R^2) of linear regression, the best-fit model was selected. Here is an expression for a pseudo-first-order equation [38]:

$$\ln(q_e - q_t) = \ln q_e - k_1 t \tag{11}$$

The variables q_t, q_e, and k_1 indicate the amount of MO adsorbed (mg/g) at time t (min), the amount adsorbed (mg/g) at equilibrium, and the adsorption constant (min^{-1}).

Equation (12) illustrates how to represent the pseudo-second-order model [38]:

$$\frac{t}{q_t} = \frac{1}{k_2 q_e^2} + \frac{1}{q_e} t \tag{12}$$

here, the adsorption constant is denoted as k_2 (g/mg min).

Weber and Morris suggest the following intra-particle mass transfer diffusion model in light of the fact that neither the pseudo-first-order nor the second-order models are able to pinpoint the diffusion mechanism:

$$q_t = k_i t^{1/2} + C \tag{13}$$

where k_i is the intra-particle diffusion rate constant (g/mg min), and C is the intercept.

The varying kinetic parameters for MO adsorption onto MLPB for a range of MO initial concentrations are displayed in Table 2. The linear plots of the first- and second-order kinetic models are displayed in Figure 10a,b. Higher correlation coefficient values ($R^2 > 0.9977$) demonstrated greater agreement between all experimental data and the pseudo-second-order kinetic model, suggesting that the latter is a more suitable fit for explaining the adsorption kinetics of MO. According to this hypothesis, chemical adsorption might be the rate-controlling step [38]. Furthermore, Table 3 shows that theoretical q_e values calculated by pseudo-second-order models are close to experimental values, while those calculated by pseudo-first-order models differ from experimental values. Many earlier studies support the findings of this study concerning second-order kinetics [38,39,45–47]. When MLPB was adsorbing MO, MO removal was rapid at first but became slower and stagnant as contact time increased. MO was removed by adsorption on the surface of MLPB due to its MO$^-$ anionic form. Adsorption kinetics are often governed by a number of processes, the most important of which are those that involve diffusion, including intra-particle, boundary layer, and external diffusion [39]. Thus, the rate-limiting stage in the adsorption process was identified using the intra-particle diffusion model. Figure 10c illustrates that across a broad range of contact periods between MO and MLPB, the linear section of the curve does not pass through the origin. This departure from the origin might be brought about by the variation in mass transfer rates between the first and last phases of adsorption. It suggests a certain amount of boundary layer control, indicating that the adsorption rate-controlling step (or all of them may be working simultaneously) is present in addition to intraparticle diffusion (or internal diffusion). The intraparticle diffusion plot's first linear section shows how a boundary layer influences adsorption, while the second linear segment shows intraparticle diffusion. As a result of C values, boundary thickness could be determined; a larger C value was associated with a greater boundary layer diffusion effect [39]. There was an increase in C values (5.10–8.12 mg/g) with increasing initial concentrations (20–60 mg/L) (Table 3), demonstrating that surface adsorption or boundary diffusion increased with concentration, implying that surface adsorption became more noticeable as concentration increased.
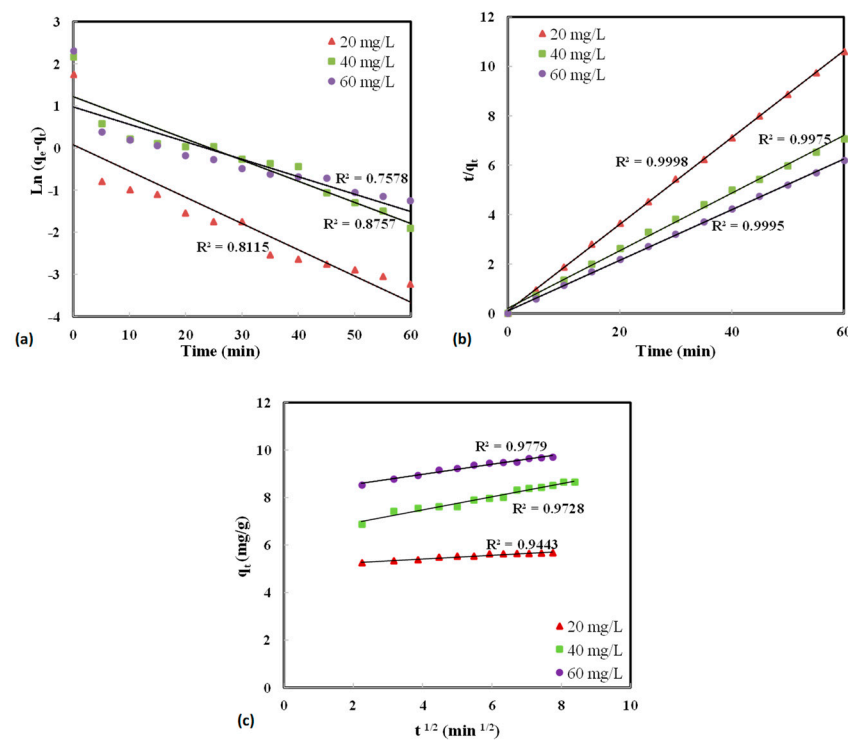
Figure 10. (**a**) Pseudo-first-order, (**b**) pseudo-second-order, and (**c**) Intraparticle diffusion kinetics plots at different initial MO concentrations.

Table 3. Rate constants for the kinetic models for various initial MO concentrations.

Initial MOCon. (mg/L)	Pseudo-First-Order Model			Pseudo-Second-Order Model			$q_{e,exp}$ (mg/g)	Intraparticle Diffusion Model		
	k_1 (min^{-1})	$q_{e,cal}$ (mg/g)	R^2	k_2 (g/mg min)	q_{cal} (mg/g)	R^2		k_i (g/mg min$^{0.5}$)	C	R^2
20	0.0623	1.08	0.8115	0.303	5.69	0.9998	5.70	0.079	5.097	0.9443
40	0.0502	3.38	0.8757	0.064	8.65	0.9975	8.59	0.2754	6.378	0.9728
60	0.0413	2.64	0.7578	0.101	9.78	0.9995	9.89	0.2121	8.123	0.9779

3.2.6. Adsorption Isotherms

In this study, three isothermal equations were used to analyze the adsorption data, namely the Langmuir, Dubinin–Radushkevich (D–R), and Freundlich isothermal equations [48]. Equations (14)–(16) give the respective linear equations of the Langmuir, D–R, and Freundlich adsorption isotherms. Langmuir's linear expression can be written as follows:

$$\frac{C_e}{q_e} = \frac{1}{Q_{max} \cdot b} + \frac{C_e}{Q_{max}} \tag{14}$$

where C_e is the equilibrium concentration (mg/L), q_e is the quantity adsorbed at equilibrium (mg/g), and Q_{max} and b are the Langmuir constants associated with the adsorption energy and capacity, respectively.

A linear expression of Freundlich's expression gives the following constants: K_F (mg/g (L/mg)$^{1/n}$) and $1/n$:

$$\log (q_e) = \log (K_F) + \left(\frac{1}{n}\right) \log (C_e) \tag{15}$$

Using the Dubinin–Radushkevich isotherm in Equation (16), the typical porosity and apparent free energy of adsorption were estimated. It is frequently employed to differentiate between the adsorbate ions' chemical and physical adsorption [48]:

$$\ln(q_e) = \ln(q_m) - \beta^2 \tag{16}$$

The variables in this equation are the Dubinin–Radushkevich monolayer capacity q_m (mg/g), the gas constant R (8.314 kJ/mol K), the Polanyi potential (ε), which is equal to $RT \ln(1 + (1 + C_e))$, the mean free energy of adsorption per mole of the adsorbate β (mol^2/kJ^2), and the absolute temperature T (K). The following Equation (17) can also be used to calculate the sorption energy.

$$E = 1/\sqrt{2\beta} \tag{17}$$

where adsorption energy mean (kJ/mol) is represented by *E*.

Figure 11a–c and Table 4 show the adsorption isotherm study plots of Langmuir, Freundlich, and D–R models, as well as their adsorption isotherm constant values, respectively. Table 4 shows that the Freundlich and D–R models are less effective at describing the data than the Langmuir model. The Langmuir model states that adsorption takes place in a monolayer, meaning that the adsorbent surface is homogenous, that only one layer of molecules is absorbed there, that the adsorption energy is constant at every site, and that the adsorbate does not move along the surface's plane [48]. Furthermore, the Langmuir model yielded maximum monolayer coverage (Q_{max}) of 17.21 mg/g. The values of $1/n = 0.637$ and $n = 1.57$ in Table 4 also indicate favorable sorption of MO on MLPB. Additionally, Table 4 shows that the obtained mean adsorption energy (*E* = 0.997 kJ/mol) indicates that physical adsorption is dominant since it is less than 8 kJ/mol. Bond energy values for monolayer, hydration water, and multilayer adsorption typically range from 4 to 21, 8 to 42, and 290 to 420 kJ/mol, respectively [48,49]. Monolayer adsorption was shown to be the predominant adsorption mode for MO adsorption on MLPB using the experiment's E value as a measure. Langmuir's linear fit, which describes the adsorption process, was consistent with this result.

Table 4. Isotherm model parameters.

T (ºC)	Langmuir Isotherm			Freundlich Isotherm			Radushkevich (D–R) Isotherm			
	b (L/mg)	Q_{max} (mg/g)	R^2	$1/n$	K_F (mg/g (L/mg)$^{1/n}$)	R^2	q_m (mg/g)	β (mol^2/kJ^2)	E (kJ/mol)	R^2
25										
	0.157	17.21	0.9986	0.637	2.13	0.9774	8.88	5×10^{-7}	0.997	0.8531

In Table 5, the maximum adsorption ability of MO is compared to that of other adsorption studies. According to this study, MLPB shows satisfactory adsorption capacity to MO dye in water solutions.

Table 5. Comparison of maximum adsorption capacity values for MO dye sorbed by different adsorbents.

Adsorbent	Q_{max} (mg/g)	Reference
Biofunctional BiOCl$_3$I solid	5.00	[50]
Modified ultrafine coal powder	18.52	[51]
Cellulose from Stipa tenacissina L	16.94	[52]
Magnetic Clay-Biochar	18.80	[8]
Carbon nanotubes	35.40	[39]

Table 5. *Cont.*

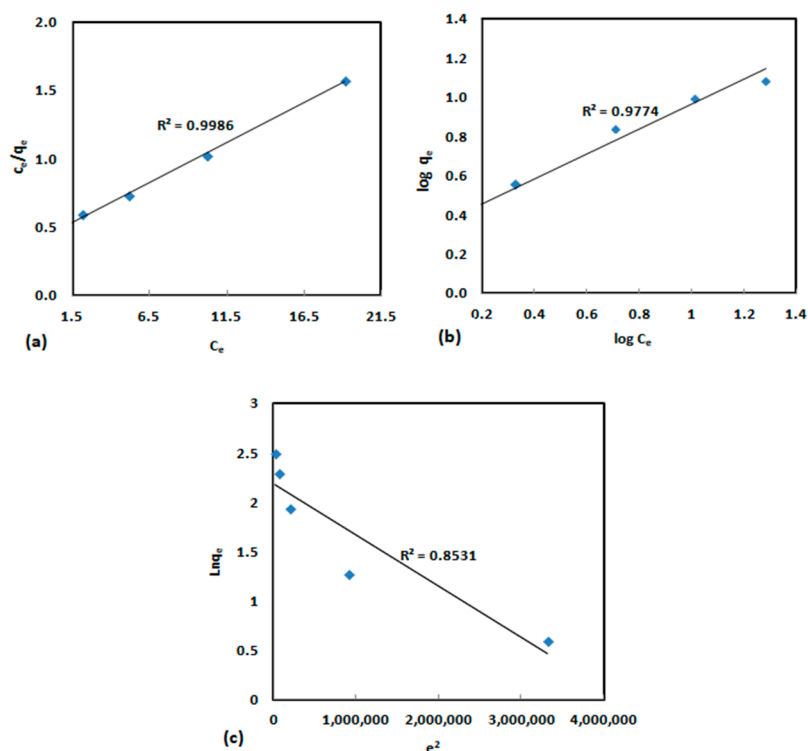| Adsorbent	Q_{max} (mg/g)	Reference
Fe_2O_3/polypeptidylated hemoglobin	15.20	[53]
Surfactant-added ZIF-8	10.10	[54]
$AgGaO_2$ nanocomposites	11.39	[55]
Fe_2O_3/biochar	16.05	[56]
MLBP	17.21	This study

Figure 11. (**a**) Langmuir, (**b**) for Freundlich, and (**c**) Dubinin–Radushkevich (D–R) isotherms plots.

3.2.7. Recycling Test

For magnetic biochar to remain viable and cost-effective over the long term, regeneration and efficiency following several adsorptions–desorption cycles are essential. The type of adsorbate and the required degree of regeneration efficiency determine the procedure to be used. The regeneration efficiency of MLPB for MO is shown in Figure 12 under four cycles. After the first adsorption–desorption cycle, 91.6% of the MO was removed by MLPB; this rate gradually declined to 87.8% after four cycles (Figure 12), which is considered an insignificant decrease. Both the breakdown of the biochar's surface structure and the disappearance of its active mineral content may contribute to a reduction in regeneration efficacy [8]. Following regeneration, changes in pore size distribution, surface chemistry, and contaminant residue cause a reduction in the removal effectiveness of magnetic biochar. In order to determine the causes of this efficiency decline, characterization of the MLPB before and after regeneration using methods including BET surface area analysis, SEM, FTIR, and chemical analysis can be conducted in the future. This aids in determining the main causes of deterioration and creating plans to enhance magnetic biochar's long-term functionality [8]. Accordingly, the MLPB used in the study has noticeable stability and can be reused for MO dye adsorption.
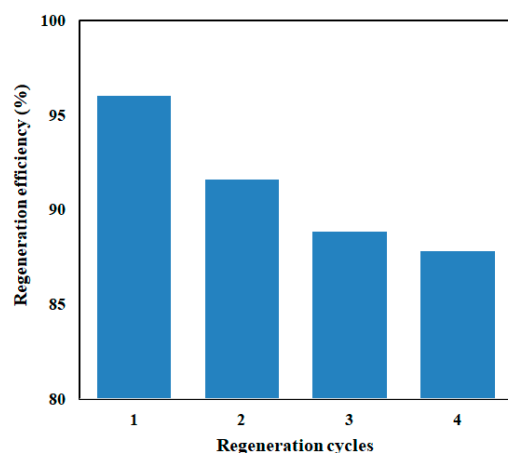
Figure 12. Recycling of MLPB for multiple adsorption-desorption of MO.

3.2.8. Column Study

In this work, three concentrations of inlet MO (20, 50, and 80 mg/L), a bed height of 1 cm, and a flow rate of 0.65 mL/min were used to investigate the impact of this dye's adsorption on MLPB. Figure 13 shows the breakthrough curves at different concentrations of influent MO. A rapid saturation of the adsorption process has been observed, and the breakthrough time has declined as the concentration of influent MO increases. Increasing MO concentration resulted in a shorter breakthrough and a higher adsorption capacity. With an increase in inlet MO concentration, the breakthrough time decreased from 270 min to 85 min, while the equilibrium uptake (q_{eq}) increased from 4.34 mg/g to 18.20 mg/g. Due to the scattering of curves of breakthrough at lesser inlet MO concentrations, a slower breakthrough occurred. As the inlet concentration increased, breakthrough curves became sharper [57]. Additionally, a smaller concentration gradient resulted in a more gentle conveyance because mass transfer or diffusion coefficients were lower. By increasing the inlet concentration, breakthrough curve slopes and shorter times are obtained [57,58]. For the removal of MO from water systems, our results demonstrate that MLPB, with a maximum equilibrium capacity of 18.20 mg/g at 0.965 column porosity, is a promising and effective adsorbent. The adsorption performance of MLPB can be considerably impacted by prolonged usage. Potential saturation changes the surface chemistry as a result of MO adsorption, and decreased surface area can all arise from this. These modifications may lessen the adsorbent's efficacy by altering its affinity for MO. For optimal operation to be maintained, regular evaluation, regeneration, and replacement are required [59].
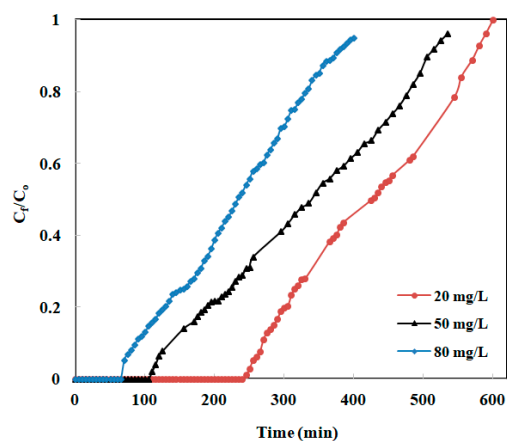

Figure 13. Breakthrough for MO at initial concentrations of 20, 50, and 80 mg/L.

3.2.9. Post-Adsorption Characterization

Figure 14 displays the FTIR spectra of MLPB both before and after MO adsorption. The main differences occurred between 1000 and 1600 cm^{-1}, where the functional groups were shifted or reduced. The absorption of C=N (1550 cm^{-1}) after adsorption was shifted to 1558, while the absorption of C–O (1047 cm^{-1}) was reduced, which suggests nitrogen and oxygen groups contributed to the adsorption process. It is evident that the amino groups in MLPB undergo a structural change when MLPB is loaded with methyl orange. As a result, the amino groups bind with the sulphonate groups of MO dye [60,61]. Additionally, the additional alkyne group peak (C=C) at 2087 cm^{-1} in the fingerprint region of MLPB was assigned to MO, supporting its attachment to the adsorbent [62]. Other changes are obviously observed at 500–1000 cm^{-1}, which are all placed in the fingerprint region. After adsorption shifting was observed in the peaks of M–O–M and O–M–O stretching, signifying the complexation between the metal ion (Fe) and SO$_3^-$ groups of MO on the MLPB surface [63].
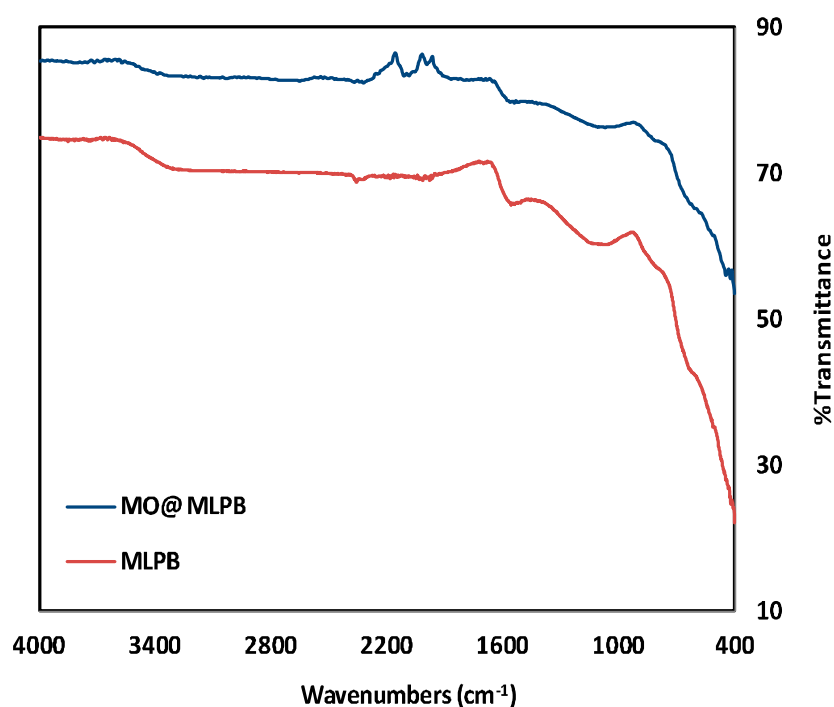

Figure 14. MLPB's FTIR before and after MO adsorption.

3.2.10. Suggested Mechanism of the Adsorption of MO onto MLPB

The suggested adsorption mechanism of MO by MLPB is illustrated in Figure 15. MO existed in an aqueous solution in the form of an anion (SO$_3^-$). The adsorption of MO was attained by electrostatic attraction or complexation, which mainly through the attraction between SO$_3^-$ and metal ions (Fe) positively charged on the MLPB surface. This was confirmed by FTIR characterization for MLPB after adsorption of MO. Obvious changes were observed at 500–1000 cm^{-1}, the peaks of M–O–M and O–M–O stretching, signifying the complexation between the metal ions (Fe) and SO$_3^-$ groups of MO on the MLPB surface [64].
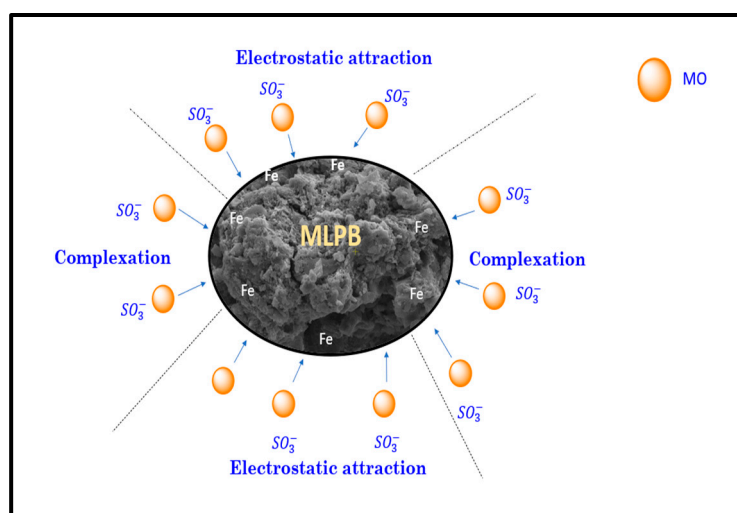
Figure 15. Suggested mechanism for adsorption of MO on MLPB.

4. Conclusions

The current investigation found that MLPB performed well as an adsorbent to remove MO from aqueous solutions. The FTIR spectrum of MLPB was found to differ from the spectrum of lemon peels, confirming the modification caused by the impregnation-pyrolysis. Further confirmation of this modification was provided by SEM analysis. When compared to the LP picture, a SEM image of the MLPB showed a porous surface. This demonstrates that the MLPB's surface shape is superior for MO ion adsorption. During batch adsorption studies, MO ion adsorption capacity has increased proportional to concentration increases, but it decreased with increasing doses and pH. The highest adsorption occurred at pH 4.0, and the optimal amount of MLPB was found to be 0.025 g within 60 min of contact time. Maximum MO removal was noted. As compared with lemon peels ($q_e = 0.54$ mg/g), MLPB displayed approximately sevenfold higher adsorption capacity ($q_e = 3.51$ mg/g). The findings indicate that, under ideal experimental circumstances, the pseudo-second-order kinetic model is the most appropriate for simulating the adsorption of MO onto the MLPB. An intra-particle diffusion model revealed that there were other rate-controlling steps besides intra-particle diffusion. The border layer influences adsorption in its early phases, whereas intra-particle diffusion is impacted in its latter stages. The Langmuir isotherm model best explained the equilibrium results. In column studies, MO adsorption on MLPB was affected by the inlet feed's MO concentration, with a maximum obtained column capacity value of 18.20 mg/g. An excellent recovery of MO was achieved through the regeneration of the synthesized adsorbent. It achieved 96% recovery in the first cycle and sustained 88% recovery after the fourth cycle. These results demonstrate the efficiency of MLPB in recovering MO from aqueous solutions and provide valuable insights into optimal adsorption conditions. MO adsorption with MLPB is a promising wastewater treatment method with several advantages over conventional methods. It provides cost-effectiveness, regenerative and reusable qualities, easy separation and recovery, and effective contamination removal. Its magnetic qualities make it easy to separate from treated wastewater, which lowers operating costs and streamlines the treatment procedure. When injected directly into polluted water bodies, MLPB may be magnetically recovered, making it appropriate for in situ applications. Additionally, it lessens the formation of sludge, which makes disposal easier and lowers related expenses and environmental issues.

Author Contributions: Conceptualization S.D.; methodology and validation, S.D., E.D. and A.T.; investigation, and resources, S.D., E.D. and A.T.; formal analysis, S.D., E.D., A.T. and M.R.E.-A.; data curation, S.D., E.D., A.T. and M.R.E.-A.; writing—original draft preparation, S.D.; writing—review and editing, S.D. and A.T.; project administration, and funding acquisition, S.D. All authors have read and agreed to the published version of the manuscript.

References

1. Dutta, S.; Gupta, B.; Srivastava, S.K.; Gupta, A.K. Recent advances on the removal of dyes from wastewater using various adsorbents: A critical review. *Mater. Adv.* **2021**, *2*, 4497–4531. [CrossRef]
2. Mohan, D.; Singh, K.P.; Singh, G.; Kumar, K. Removal of dyes from wastewater using flyash, a low-cost adsorbent. *Ind. Eng. Chem. Res.* **2002**, *41*, 3688–3695. [CrossRef]
3. Bilal, M.; Ihsanullah, I.; Shah, M.U.; Reddy, A.V.; Aminabhavi, T.M. Recent advances in the removal of dyes from wastewater using low-cost adsorbents. *J. Environ. Manag.* **2022**, *321*, 115981. [CrossRef] [PubMed]
4. Singh, P.K.; Singh, R.L. Bio-removal of azo dyes: A review. *Int. J. Appl. Sci. Biotechnol.* **2017**, *5*, 108–126. [CrossRef]
5. Mittal, A.; Malviya, A.; Kaur, D.; Mittal, J.; Kurup, L. Studies on the adsorption kinetics and isotherms for the removal and recovery of Methyl Orange from wastewaters using waste materials. *J. Hazard. Mater.* **2007**, *148*, 229–240. [CrossRef]
6. Wang, S.S.; Yan, Y.M.; Hsu, C.H.; Lin, H.P. Waste bamboo-derived biochar and multiporous carbon as adsorbents for methyl orange removal. *J. Chin. Chem. Soc.* **2023**, *70*, 1628–1635. [CrossRef]
7. Hambisa, A.A.; Regasa, M.B.; Ejigu, H.G.; Senbeto, C.B. Adsorption studies of methyl orange dye removal from aqueous solution using Anchote peel-based agricultural waste adsorbent. *Appl. Water Sci.* **2023**, *13*, 24. [CrossRef]
8. Zhao, F.; Shan, R.; Li, S.; Yuan, H.; Chen, Y. Characterization and Co-adsorption mechanism of magnetic clay-biochar composite for de-risking Cd(II) and methyl orange contaminated water. *Int. J. Mol. Sci.* **2023**, *24*, 5755. [CrossRef]
9. Al-Kazragi, M.A.; Al-Heetimi, D.T.; Wilson, L.D. Adsorption of methyl orange on low-cost adsorbent natural materials and modified natural materials: A review. *Int. J. Phytoremed.* **2024**, *26*, 639–668. [CrossRef]
10. Taktak, F.; Gökçe, S. Ultrasound-assisted synthesis of biodegradable graphene oxide-based hydrogel nanocomposites for highly efficient and cost-effective removal of methyl orange from aqueous media. *J. Water Process Eng.* **2024**, *58*, 104837. [CrossRef]
11. Ren, Z.; Chen, F.; Wang, B.; Song, Z.; Zhou, Z.; Ren, D. Magnetic biochar from alkali-activated rice straw for removal of rhodamine B from aqueous solution. *Environ. Eng. Res.* **2020**, *25*, 536–544. [CrossRef]
12. Reddy, D.H.K.; Lee, S. Magnetic biochar composite: Facile synthesis, characterization, and application for heavy metal removal. *Colloids Surf. A* **2014**, *454*, 96–103. [CrossRef]
13. Feng, Z.; Yuan, R.; Wang, F.; Chen, Z.; Zhou, B.; Chen, H. Preparation of magnetic biochar and its application in catalytic degradation of organic pollutants: A review. *Sci. Total Environ.* **2021**, *765*, 142673. [CrossRef]
14. Mohan, D.; Kumar, H.; Sarswat, A.; Alexandre-Franco, M.; Pittman, C.U. Cadmium and lead remediation using magnetic oak wood and oak bark fast pyrolysis bio-chars. *Chem. Eng. J.* **2014**, *236*, 513–528. [CrossRef]
15. Nodeh, H.R.; Ibrahim, W.A.W.; Ali, I.; Sanagi, M.M. Development of magnetic graphene oxide adsorbent for the removal and preconcentration of As (III) and As (V) species from environmental water samples. *Environ. Sci. Pollut. R* **2016**, *23*, 9759–9773. [CrossRef] [PubMed]
16. Gan, Q.; Hou, H.; Liang, S.; Qiu, J.; Tao, S.; Yang, L.; Yu, W.; Xiao, K.; Liu, B.; Hu, J.; et al. Sludge-derived biochar with multivalent iron as an efficient Fenton catalyst for degradation of 4-Chlorophenol. *Sci. Total Environ.* **2020**, *725*, 138299. [CrossRef]
17. Bai, S.; Li, R.; Su, G.; Duan, X.; Wang, S.; Ren, N.Q.; Ho, S.H. Magnetic biochar catalysts from anaerobic digested sludge: Production, application and environment impact. *Environ. Int.* **2019**, *126*, 302–308.
18. Jones, T.C. State of nature: The politics of water in the making of Saudi Arabia. In *Water on Sand: Environmental Histories of the Middle East and North Africa*; Oxford University Press: New York, NY, USA, 2013; pp. 231–250.
19. Jitjamnong, J.; Thunyaratchatanon, C.; Luengnaruemitchai, A.; Kongrit, N.; Kasetsomboon, N.; Sopajarn, A.; Chuaykarn, N.; Khantikulanon, N. Response surface optimization of biodiesel synthesis over a novel biochar-based heterogeneous catalyst from cultivated (*Musa sapientum*) banana peels. *Biomass Convers. Biorefinery* **2021**, *11*, 2795–2811. [CrossRef]
20. Amin, M.T.; Alazba, A.A.; Shafiq, M. Removal of copper and lead using banana biochar in batch adsorption systems: Isotherms and kinetic studies. *Arab. J. Sci. Eng.* **2018**, *43*, 5711–5722. [CrossRef]
21. Luo, X.; Deng, Z.; Lin, X.; Zhang, C. Fixed-bed column study for Cu^{2+} removal from solution using expanding rice husk. *J. Hazard. Mater.* **2011**, *187*, 182–189. [CrossRef]
22. Zhang, W.; Thompson, K.E.; Reed, A.H.; Beenken, L. Relationship between packing structure and porosity in fixed beds of equilateral cylindrical particles. *Chem. Eng. Sci.* **2006**, *61*, 8060–8074. [CrossRef]
23. Ahmad, M.A.; Ahmad, N.; Bello, O.S. Adsorption kinetic studies for the removal of synthetic dye using durian seed activated carbon. *J. Dispers. Sci. Technol.* **2015**, *36*, 670–684. [CrossRef]
24. Urgel, J.J.; Briones, J.M.; Diaz, E.B., Jr.; Dimaculangan, K.M.; Rangel, K.L.; Lopez, E.C. Removal of diesel oil from water using biochar derived from waste banana peels as adsorbent. *Carbon Res.* **2024**, *3*, 13. [CrossRef]

25. Sheng, Z.; Shen, Y.; Dai, H.; Pan, S.; Ai, B.; Zheng, L.; Zheng, X.; Xu, Z. Physicochemical characterization of raw and modified banana pseudostem fibers and their adsorption capacities for heavy metal Pb^{2+} and Cd^{2+} in water. *Polym. Compos.* **2018**, *39*, 1869–1877. [CrossRef]

26. Park, J.H.; Wang, J.J.; Meng, Y.; Wei, Z.; DeLaune, R.D.; Seo, D.C. Adsorption/desorption behavior of cationic and anionic dyes by biochars prepared at normal and high pyrolysis temperatures. *Colloids Surf. A* **2019**, *572*, 274–282. [CrossRef]

27. Chaukura, N.; Murimba, E.C.; Gwenzi, W. Synthesis, characterisation and methyl orange adsorption capacity of ferric oxide–biochar nano-composites derived from pulp and paper sludge. *Appl. Water Sci.* **2017**, *7*, 2175–2186. [CrossRef]

28. Mittal, H.; Mishra, S.B. Gum ghatti and Fe_3O_4 magnetic nanoparticles based nanocomposites for the effective adsorption of rhodamine B. *Carbohydr. Polym.* **2014**, *101*, 1255–1264. [CrossRef]

29. Jia, Y.; Zhang, Y.; Fu, J.; Yuan, L.; Li, Z.; Liu, C.; Zhao, D.; Wang, X. A novel magnetic biochar/MgFe-layered double hydroxides composite removing Pb^{2+} from aqueous solution: Isotherms, kinetics and thermodynamics. *Colloids Surf. A Physicochem. Eng. Asp.* **2019**, *567*, 278–287. [CrossRef]

30. Devi, S.; Sharma, V.; Chahal, S.; Goel, P.; Singh, S.; Kumar, A.; Kumar, P. Phase transformation and structural evolution in iron oxide nanostructures. *Mater. Sci. Eng. B* **2021**, *272*, 115329.

31. Dewage, N.B.; Liyanage, A.S.; Pittman, C.U., Jr.; Mohan, D.; Mlsna, T. Fast nitrate and fluoride adsorption and magnetic separation from water on α-Fe_2O_3 and Fe_3O_4 dispersed on Douglas fir biochar. *Bioresour. Technol.* **2018**, *263*, 258–265. [CrossRef]

32. Zhang, M.; Gao, B.; Varnoosfaderani, S.; Hebard, A.; Yao, Y.; Inyang, M. Preparation and characterization of a novel magnetic biochar for arsenic removal. *Bioresour. Technol.* **2013**, *130*, 457–462. [CrossRef] [PubMed]

33. Cheng, W.; Tang, K.; Qi, Y.; Sheng, J.; Liu, Z. One-step synthesis of superparamagnetic monodisperse porous Fe_3O_4 hollow and core-shell spheres. *J. Mater. Chem.* **2010**, *20*, 1799–1805. [CrossRef]

34. Hosny, M.; Fawzy, M.; Eltaweil, A.S. Green synthesis of bimetallic Ag/ZnO@Biohar nanocomposite for photocatalytic degradation of tetracycline, antibacterial and antioxidant activities. *Sci. Rep.* **2022**, *12*, 7316. [CrossRef]

35. Hossain, N.; Nizamuddin, S.; Griffin, G.; Selvakannan, P.; Mubarak, N.M.; Mahlia, T.M. Synthesis and characterization of rice husk biochar via hydrothermal carbonization for wastewater treatment and biofuel production. *Sci. Rep.* **2020**, *10*, 18851. [CrossRef]

36. Lowell, S.; Shields, J.E.; Thomas, M.A.; Thommes, M. *Characterization of Porous Solids and Powders: Surface Area, Pore Size and Density*; Springer Science & Business Media: Berlin/Heidelberg, Germany, 2006.

37. Hameed, B.H.; Ahmad, A.A.; Aziz, N. Isotherms, kinetics and thermodynamics of acid dye adsorption on activated palm ash. *Chem. Eng. J.* **2007**, *133*, 195–203. [CrossRef]

38. Cordova Estrada, A.K.; Cordova Lozano, F.; Lara Díaz, R.A. Thermodynamics and kinetic studies for the adsorption process of methyl orange by magnetic activated carbons. *Air Soil Water Res.* **2021**, *14*, 11786221211013336. [CrossRef]

39. Yao, Y.; Bing, H.; Feifei, X.; Xiaofeng, C. Equilibrium and kinetic studies of methyl orange adsorption on multiwalled carbon nanotubes. *Chem. Eng. J.* **2011**, *170*, 82–89. [CrossRef]

40. Zhang, L.; Hu, P.; Wang, J.; Liu, Q.; Huang, R. Adsorption of methyl orange (MO) by Zr(IV)-immobilized cross-linked chitosan/bentonite composite. *Int. J. Biol. Macromol.* **2015**, *81*, 818–827. [CrossRef]

41. Zhang, L.; Tu, L.Y.; Liang, Y.; Chen, Q.; Li, Z.S.; Li, C.H.; Wang, Z.H.; Li, W. Coconut-based activated carbon fibers for efficient adsorption of various organic dyes. *RSC Adv.* **2018**, *8*, 42280–42291. [CrossRef]

42. Kubendiran, H.; Hui, D.; Pulimi, M.; Chandrasekaran, N.; Murthy, P.S.; Mukherjee, A. Removal of methyl orange from aqueous solution using SRB supported Bio-Pd/Fe NPs. *Environ. Nanotechnol. Monit. Manag.* **2021**, *16*, 100561. [CrossRef]

43. Han, L.; Xue, S.; Zhao, S.; Yan, J.; Qian, L.; Chen, M. Biochar supported nanoscale iron particles for the efficient removal of methyl orange dye in aqueous solutions. *PLoS ONE* **2015**, *10*, e0132067. [CrossRef] [PubMed]

44. El Maguana, Y.; Elhadiri, N.; Benchanaa, M.; Chikri, R. Adsorption Thermodynamic and Kinetic Studies of Methyl Orange onto Sugar Scum Powder as a Low-Cost Inorganic Adsorbent. *J. Chem.* **2020**, *2020*, 9165874. [CrossRef]

45. Zhang, B.; Wu, Y.; Cha, L. Removal of methyl orange dye using activated biochar derived from pomelo peel wastes: Performance, isotherm, and kinetic studies. *J. Dispers. Sci. Technol.* **2020**, *41*, 125–136. [CrossRef]

46. Bekhoukh, A.; Moulefera, I.; Zeggai, F.Z.; Benyoucef, A.; Bachari, K. Anionic methyl orange removal from aqueous solutions by activated carbon reinforced conducting polyaniline as adsorbent: Synthesis, characterization, adsorption behavior, regeneration and kinetics study. *J. Polym. Environ.* **2022**, *30*, 886–895. [CrossRef]

47. Hussain, S.; Kamran, M.; Khan, S.A.; Shaheen, K.; Shah, Z.; Suo, H.; Khan, Q.; Shah, A.B.; Rehman, W.U.; Al-Ghamdi, Y.O.; et al. Adsorption, kinetics and thermodynamics studies of methyl orange dye sequestration through chitosan composites films. *Int. J. Biol. Macromol.* **2021**, *168*, 383–394. [CrossRef]

48. Saadi, R.; Saadi, Z.; Fazaeli, R.; Fard, N.E. Monolayer and multilayer adsorption isotherm models for sorption from aqueous media. *Korean J. Chem. Eng.* **2015**, *32*, 787–799. [CrossRef]

49. Annadurai, G.; Juang, R.S.; Lee, D.J. Use of cellulose-based wastes for adsorption of dyes from aqueous solutions. *J. Hazard. Mater.* **2002**, *92*, 263–274. [CrossRef]

50. Zhang, Y.; Sun, X.; Yang, G.; Zhu, Y.; Si, H.; Zhang, J.; Li, Y. Preparation and characterization of bifunctional $BiOCl_xI_y$ solid solutions with excellent adsorption and photocatalytic abilities for removal of organic dyes. *Mater. Sci. Semicond. Process.* **2016**, *41*, 193–199. [CrossRef]

51. Liu, Z.; Zhou, A.; Wang, G.; Zhao, X. Adsorption behavior of methyl orange onto modified ultrafine coal powder. *Chin. J. Chem. Eng.* **2009**, *17*, 942–948.

52. Lafi, R.; Abdellaoui, L.; Montasser, I.; Hafiane, A. Removal of methyl orange from aqueous solution onto modified extracted cellulose from *Stipa tenacissima* L. *Int. J. Environ. Anal. Chem.* **2022**, *102*, 8124–8140. [CrossRef]

53. Matthew, E.; Roshelle, G.M. Simultaneous adsorption of acidic and basic dyes onto magnetized polypeptidylated-hemoglobin composites. *Sep. Purif. Technol.* **2021**, *255*, 117701.

54. Tran, B.L.; Chin, H.Y.; Chang, B.K.; Chiang, A.S. Dye adsorption in ZIF-8: The importance of external surface area. *Microporous Mesoporous Mater.* **2019**, *277*, 149–153. [CrossRef]

55. Alhaji, N.M.; Nathiya, D.; Kaviyarasu, K.; Meshram, M.; Ayeshamariam, A. A comparative study of structural and photocatalytic mechanism of AgGaO2 nanocomposites for equilibrium and kinetics evaluation of adsorption parameters. *Surf. Interfaces* **2019**, *17*, 100375. [CrossRef]

56. Shang, Y.; Li, X.; Yang, Y.; Wang, N.; Zhuang, X.; Zhou, Z. Optimized photocatalytic regeneration of adsorption-photocatalysis bifunctional composite saturated with Methyl Orange. *J. Environ. Sci.* **2020**, *94*, 40–51. [CrossRef]

57. Fallah, N.; Taghizadeh, M. Continuous fixed-bed adsorption of Mo (VI) from aqueous solutions by Mo (VI)-IIP: Breakthrough curves analysis and mathematical modeling. *J. Environ. Chem. Eng.* **2020**, *8*, 104079. [CrossRef]

58. Zhang, W.; Yan, H.; Li, H.; Jiang, Z.; Dong, L.; Kan, X.; Yang, H.; Li, A.; Cheng, R. Removal of dyes from aqueous solutions by straw based adsorbents: Batch and column studies. *Chem. Eng. J.* **2011**, *168*, 1120–1127. [CrossRef]

59. Wang, L.; Shi, C.; Pan, L.; Zhang, X.; Zou, J.J. Rational design, synthesis, adsorption principles and applications of metal oxide adsorbents: A review. *Nanoscale* **2020**, *12*, 4790–4815. [CrossRef]

60. Alyasi, H.; Mackey, H.; McKay, G. Adsorption of methyl orange from water using chitosan bead-like materials. *Molecules* **2023**, *28*, 6561. [CrossRef]

61. Allouche, F.N.; Yassaa, N.; Lounici, H. Sorption of methyl orange from aqueous solution on chitosan biomass. *Procedia Earth Planet. Sci.* **2015**, *15*, 596–601. [CrossRef]

62. Al-Odayni, A.B.; Alsubaie, F.S.; Saeed, W.S. Nitrogen-rich polyaniline-based activated carbon for water treatment: Adsorption kinetics of anionic dye methyl orange. *Polymers* **2023**, *15*, 806. [CrossRef]

63. El Hassani, K.; Beakou, B.H.; Kalnina, D.; Oukani, E.; Anouar, A. Effect of morphological properties of layered double hydroxides on adsorption of azo dye Methyl Orange: A comparative study. *Appl. Clay Sci.* **2017**, *140*, 124–131. [CrossRef]

64. Wang, J.; Chen, W.; Zhang, M.; Zhou, R.; Li, J.; Zhao, W.; Wang, L. Optimize the preparation of Fe_3O_4-modified magnetic mesoporous biochar and its removal of methyl orange in wastewater. *Environ. Monit. Assess.* **2021**, *193*, 1–20. [CrossRef] [PubMed]